

Article

Revealing the Real Role of Etching during Controlled Assembly of Nanocrystals Applied to Electrochemical Reduction of CO₂

Tingting Yue, Ying Chang *, Haitao Huang, Jingchun Jia * and Meilin Jia

College of Chemistry and Environmental Science, Inner Mongolia Key Laboratory of Green Catalysis and Inner Mongolia Collaborative Innovation Center for Water Environment Safety, Inner Mongolia Normal University, Hohhot 010022, China; yuett9707@163.com (T.Y.); huanght2022@163.com (H.H.); jml@imnu.edu.cn (M.J.)

* Correspondence: changying@imnu.edu.cn (Y.C.); jjc1983@126.com (J.J.)

Abstract: In recent years, the use of inexpensive and efficient catalysts for the electrocatalytic CO₂ reduction reaction (CO₂RR) to regulate syngas ratios has become a hot research topic. Here, a series of nitrogen-doped iron carbide catalysts loaded onto reduced graphene oxide (N-Fe₃C/rGO-H) were prepared by pyrolysis of iron oleate, etching, and nitrogen-doped carbonization. The main products of the N-Fe₃C/rGO-H electrocatalytic reduction of CO₂ are CO and H₂, when tested in a 0.5 M KHCO₃ electrolyte at room temperature and pressure. In the prepared catalysts, the high selectivity (the Faraday efficiency of CO was 40.8%, at −0.3 V), and the total current density reaches ~29.1 mA/cm² at −1.0 V as demonstrated when the mass ratio of Fe₃O₄ NPs to rGO was equal to 100, the nitrogen doping temperature was 800 °C and the ratio of syngas during the reduction process was controlled by the applied potential (−0.2~−1.0 V) in the range of 1 to 20. This study provides an opportunity to develop nonprecious metals for the electrocatalytic CO₂ reduction reaction preparation of synthesis and gas provides a good reference

Keywords: N-Fe₃C/rGO-H; electrochemical CO₂ reduction; synergistic effect



Citation: Yue, T.; Chang, Y.; Huang, H.; Jia, J.; Jia, M. Revealing the Real Role of Etching during Controlled Assembly of Nanocrystals Applied to Electrochemical Reduction of CO₂. *Nanomaterials* **2022**, *12*, 2546. <https://doi.org/10.3390/nano12152546>

Academic Editors: Fabrizio Pirri and Ioannis V. Yentekakis

Received: 21 April 2022

Accepted: 20 July 2022

Published: 24 July 2022

Publisher's Note: MDPI stays neutral with regard to jurisdictional claims in published maps and institutional affiliations.



Copyright: © 2022 by the authors. Licensee MDPI, Basel, Switzerland. This article is an open access article distributed under the terms and conditions of the Creative Commons Attribution (CC BY) license (<https://creativecommons.org/licenses/by/4.0/>).

1. Introduction

The Earth's temperature is rising, and extreme weather, forest fires and ice shelf collapses are a growing problem. Curbing climate warming has become an urgent issue for the international community. CO₂, as the most dominant greenhouse gas, is considered to be the breakthrough point to curb warming. The concept of "carbon neutrality" was born. Among the many carbon neutral technology pathways, there is one governance idea that has attracted particular attention due to its high efficiency in reducing CO₂ concentrations in the atmosphere, namely, carbon capture and resource utilization. CO₂ is an extremely stable molecule that is involved in chemical synthesis as a raw material and requires the absorption of large amounts of energy [1]. Therefore, transforming CO₂ into syngas under mild conditions is an urgent need for protecting the environment and reducing energy consumption. [2]. The electrocatalytic CO₂ reduction reaction (CO₂RR) is mild, does not require high temperature and pressure and only requires electricity consumed from sustainable energy sources to convert CO₂ to CO [3,4]. In addition, some electricity waste is inevitable due to the cyclical nature of solar and wind power [5]. This process is economically feasible through the use of excess CO₂ and waste electricity [6–8].

CO₂RR in aqueous solution is always combined with hydrogen evolution reaction (HER); therefore, H⁺ in water is used as a source of hydrogen to prepare syngas [9–11]. Syngas is a mixture of hydrogen (H₂) and carbon monoxide (CO) that can be used as a raw material or intermediate in chemical synthesis, such as Fischer–Tropsch synthesis for the preparation of alcohols and olefins. In recent years, researchers have designed a large number of catalysts for the preparation of syngas from CO₂RR [12,13]. Precious metals, such as Au [14], Ag [15] and Pd₃Bi [16], and other metals, such as Zn [17], Pb/CNT [18], Co₃O₄-CDots-C₃N₄ [19], CdS_xSe_{1-x} [20], E-MoS₂ [21] and Cu-Sn alloys [22], have been

reported, with the latter making great progress. For example, Zou et al. [23] reported Ni-Co double monoatomic loading to carbon nanotubes for the preparation of syngas with CO/H₂ ratios between 1.3 and 1.5 and Ni-N₄ and Co-N₄ as the active sites for the CO₂RR and HER, respectively. Wang's group [8] converted CO₂ to syngas by selective phosphorylation of reduced partial Cu₃P nanowires, and the vacancies created by phosphorylation accelerated charge transfer and significantly improved the activity and selectivity of CO₂. However, achieving high current density applications in aqueous solutions is still difficult in practice and limited in scale due to the small reserves of precious metals in the Earth's crust. Therefore, the search for catalysts that are inexpensive and suitable for application in CO conversion to H₂/CO in Fischer–Tropsch synthesis is urgent.

Among many nonprecious metals, carbon-based materials intrigue researchers in CO₂RR due to their cheap price, large specific surface area and high electrical conductivity [24,25]. In particular, transition metals loaded onto N-doped carbon substrates (M-N-C) have attracted the attention of researchers as new materials. Zhao et al. [26] prepared a series of Fe-N-C catalysts to control the ratio of H₂/CO in the range of 4:1 to 1:3. Yue et al. [27] designed the in situ loading of Fe-Ni alloys onto N-doped carbon substrates by changing the applied potential and adjusting the Fe-Ni molar ratio to flexibly modulate the syngas ratio. Jia's group [28] developed a N-Fe₃C/rGO catalyst for CO₂RR syngas preparation and found that the synergistic effect of C-N and Fe-N facilitated CO generation, while rGO as a carrier improved the electrical conductivity. To date, M-N-C catalysts for oxygen reduction reactions have also shown efficient catalytic activity [29,30]. Although M-N-C for CO₂RR can produce CO, HCOOH and C₂H₄ [31–33], there are relatively few studies based on low-cost M-N-C materials to investigate the ratio of syngas fractions through adjustment of the applied electric potential. Here, we prepared Fe₃O₄ NPs using iron oleate precursors and assembled them into rGO with different mass ratios and then doped with nitrogen at different temperatures to investigate the effects of Fe₃O₄/rGO and nitrogen doping temperature on the CO₂RR. The catalysts prepared at mass ratio of 100 and 800 °C were applied to the CO₂RR, showing good activity and selectivity.

2. Results and Discussion

The iron oleate precursors were first prepared using FeCl₃·6H₂O and NaOA oil baths, and the precursors were pyrolyzed to generate Fe₃O₄ NPs [34], which would be assembled into rGO with different mass ratios of nanoparticles, as shown in Figure S1. The SEM images of Fe₃O₄/rGO obtained after using HCl etching to obtain Fe₃O₄/rGO-H are shown in Figure S2. The successful loading of Fe₃O₄ onto the rGO surface can be observed from the SEM image. Comparing the distribution of Fe₃O₄ NPs on the rGO surface before and after etching, it was found that the NPs discretely stacked and then agglomerated with increasing nanoparticle loading before etching; after strong acid etching, the number of nanoparticles decreased significantly, and a hole-like structure appeared. The addition of a nitrogen source continued the sintering at high temperature, and it was found that the dispersion of nanoparticles was better at 800 °C with an Fe₃O₄/rGO mass ratio of 100, and agglomeration started to occur at 120, as illustrated Figure 1. Comparison of the SEM images for different nitrogen doping temperatures showed no influence of temperature on the morphology of the catalyst.

Figure 2a,b show the XRD patterns of Fe₃O₄/rGO before and after etching with strong acid. The diffraction peaks are located at 30.0°, 35.4°, 43.1°, 56.9° and 62.5° according to the (220), (311), (400), (511) and (440) Fe₃O₄ crystal planes (PDF#99-0073), respectively. It was observed that the crystal planes did not change before and after etching, but the peak intensity was slightly weakened. XRD patterns of N-Fe₃C/rGO-H obtained by calcination of Fe₃O₄/rGO doped with dicyandiamine at high temperature are shown in Figure 2c. The 2θ positions of the peaks are at 26.4°, 37.6°, 39.8°, 40.6°, 42.8°, 43.7°, 44.5°, 44.9°, 45.8°, 49.1°, 51.8°, 54.4°, 58.4° and 70.8° corresponding to Fe₃C's (020), (121), (002), (201), (211) (102), (220), (031), (112), (221), (122), (230), (231) and (123) sides of Fe₃C (PDF#35-1-0772), respectively. The XRD results demonstrate the successful preparation of Fe₃O₄ NPs by

pyrolysis of iron oleate precursors, which were converted to Fe_3C by sintering at high temperature after nitrogen doping. The XRD of the comparison samples N- $\text{Fe}_3\text{C}/\text{rGO-H-700}$ and N- $\text{Fe}_3\text{C}/\text{rGO-H-900}$ are shown in Figure S3, and the calcination temperature has no effect on the formation of the crystalline phase of Fe_3C .

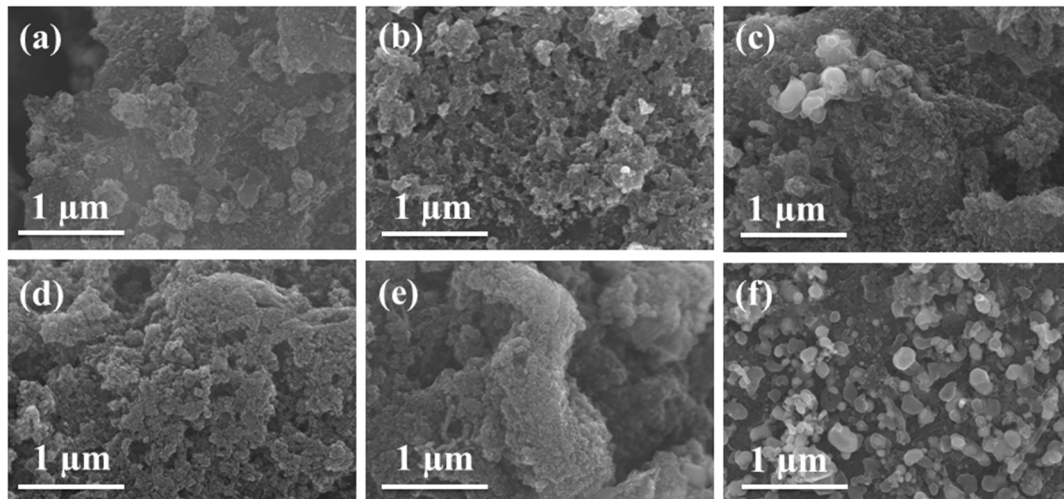


Figure 1. SEM images of (a) N- $\text{Fe}_3\text{C}/\text{rGO-H-80}$, (b) N- $\text{Fe}_3\text{C}/\text{rGO-H-100}$, (c) N- $\text{Fe}_3\text{C}/\text{rGO-H-120}$, (d) N- $\text{Fe}_3\text{C}/\text{rGO-H-700}$, (e) N- $\text{Fe}_3\text{C}/\text{rGO-H-900}$, and (f) N- $\text{Fe}_3\text{C-H}$.

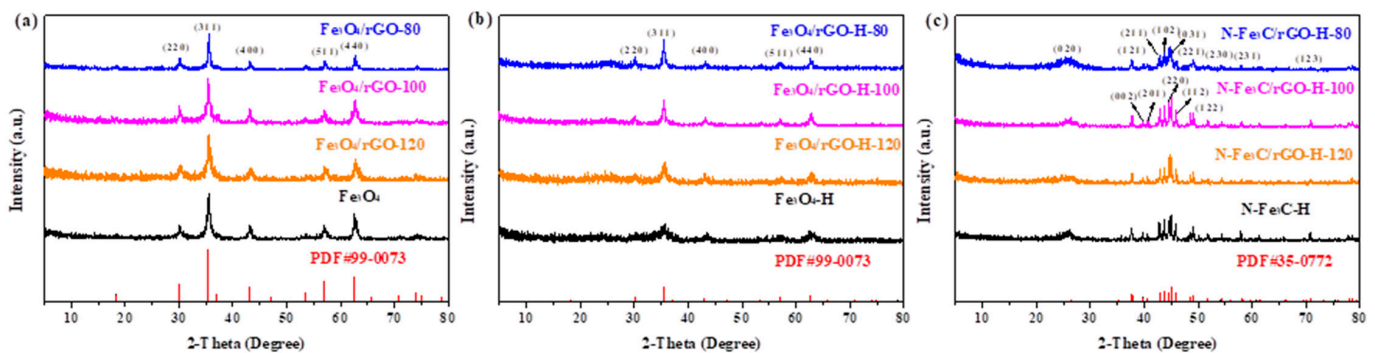


Figure 2. XRD patterns of (a) $\text{Fe}_3\text{O}_4/\text{rGO}$, (b) $\text{Fe}_3\text{O}_4/\text{rGO-H}$ and (c) N- $\text{Fe}_3\text{C}/\text{rGO-H}$.

TEM further observed the morphological changes of $\text{Fe}_3\text{O}_4/\text{rGO}$ before and after strong acid etching and nitrogen-doped high-temperature calcination. Figure 3a shows the integration of nanoparticles on the carrier surface after calcination of Fe_3O_4 NPs and rGO components at 500°C . Since the number of nanoparticles anchored on the carrier surface was limited, the excess and poorly anchored particles on the rGO surface were etched off with 1 M HCl, as shown in Figure 3d. Observation of the pictures revealed that the remaining Fe_3O_4 NPs were more uniformly dispersed on the carrier surface after the accumulation of particles in rGO was successfully etched off. Then, dicyandiamide was added and scorched at 800°C . The Fe atoms overflowed on the rGO surface, leaving a hollow shell (Figure 3g). These shell structures may become the active sites of the CO_2RR . In addition, the $\text{Fe}_3\text{O}_4/\text{rGO-100}$ and $\text{Fe}_3\text{O}_4/\text{rGO-H-100}$ grain sizes are approximately 10.2 ± 1.2 nm and 9.73 ± 1.2 nm, respectively, and the grain size of the empty shells is approximately 6.74 ± 1.2 nm. The grain size data indicate that the decrease in the number of iron atoms on the substrate and the high-temperature carbonization cause the nanoparticle size and the size of the empty shells to gradually decrease. By measuring the lattice stripes in the HRTEM of $\text{Fe}_3\text{O}_4/\text{rGO-100}$, $\text{Fe}_3\text{O}_4/\text{rGO-H-100}$ and N- $\text{Fe}_3\text{C}/\text{rGO-H-100}$ as 0.241 nm, 0.200 nm and 0.288 nm, 0.195 nm responding to the (222), (400), (220) planes of Fe_3O_4 and (112) faces of Fe_3C , respectively. The diffraction rings of Figure 3c,f,i illustrate that all three nanoparticles are polycrystalline in structure. The energy-dispersive X-ray spectroscopy

(EDS) of N-Fe₃C/rGO-H-100 clearly shows that C, Fe and N are uniformly distributed on the rGO surface (Figure 3j–m).

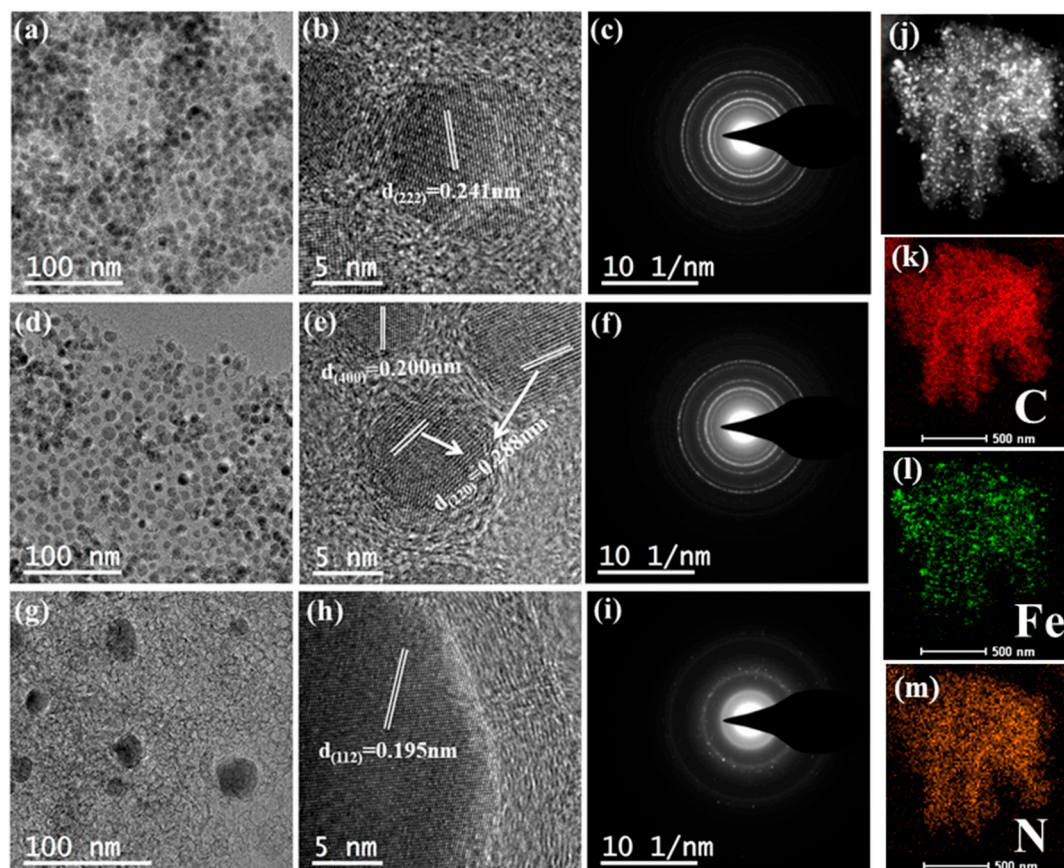


Figure 3. TEM images of (a–c) Fe₃O₄/rGO-100, (d–f) Fe₃O₄/rGO-H-100 and (g–i) N-Fe₃C/rGO-H-100. (j–m) EDS mapping of C, Fe and N in N-Fe₃C/rGO-H-100.

The interaction between rGO and Fe₃C was studied and the Raman spectra of the catalysts were determined (Figure S4). One band at approximately 1350 cm⁻¹ (D-band) corresponds to the hexagonal graphene plane in the samples tested. Another band at about 1586 and 1580 cm⁻¹ (G-band) is attributed to defects in N-Fe₃C/rGO-H-100, and rGO, respectively [35]. I_D/I_G (the ratio of D-band to G-band intensity) is used to measure the disorder of carbon materials [36]. The I_D/I_G value of N-Fe₃C/rGO-H-100 (1.03) is greater than that of rGO, suggesting that the loading of Fe₃C onto the carbon-based material leads to an increase in disorder leading to an increase in defects and the acquisition of more active sites thus improving the performance of CO₂RR [26].

Using XPS to understand the composition and valence of the catalyst, it can be seen from Figure 4a that it mainly contains four elements, C, N, Fe and O, without other spurious peaks, in agreement with the mapping results. As shown in Figure 4b, the fine spectra of C1s coincide with peaks positioned at 284.6, 285.7 and 286.6 eV, corresponding to C=C, C-N and C=O, respectively [37]. The characteristic peaks of the high-resolution spectra of N1s were located at 398.5, 399.7, 400.8 and 403.9 eV, corresponding to pyridine N, Fe-N, graphite N and oxidized N, respectively, as shown in Figure 4c [38,39]. The Fe-N peak is observed at 399.7 eV, indicating that an iron atom is coupled with two N atoms [40]. Figure 4d exhibits the Fe 2P spectrum of N-Fe₃C/rGO-H-100. The binding energies at 710.3 and 723.2 eV would correspond to 2P_{3/2} and 2P_{1/2} of Fe²⁺; those located at 713.4 and 725.4 eV would correspond to 2P_{3/2} and 2P_{1/2} of Fe³⁺ [41]. Furthermore, 710.3 eV is also considered the chemical shift of Fe coordinated to N, which is consistent with the analysis of N1s. Fe-N_X provides N doping that provides strong evidence and can enhance the charge transfer

between rGO and Fe [30,42,43]. The peak at 707.8 eV can be considered the peak of Fe⁰ or iron carbide, and the weaker peak intensity is due to the low density of metallic iron agglomerates and the encapsulation of the FeN_x active site by the carbon substrate [44–46].

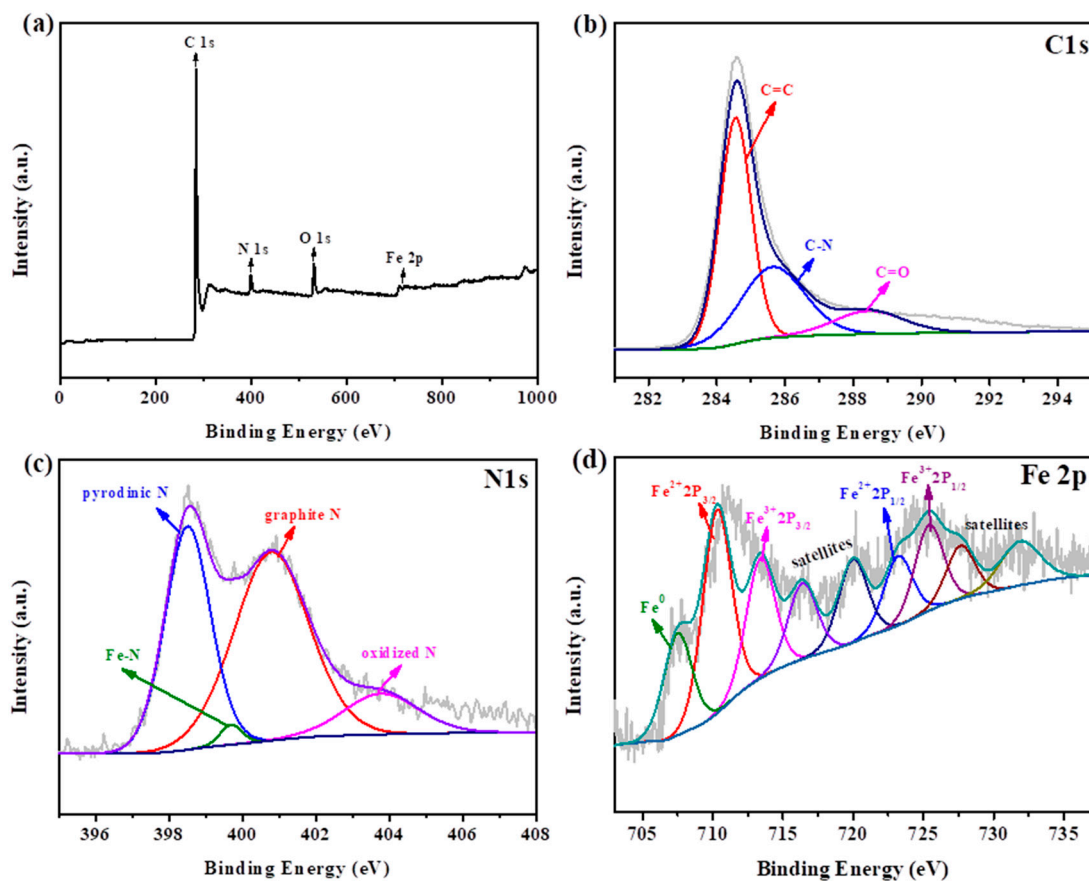


Figure 4. XPS spectra of N-Fe₃C/rGO-H-100: (a) survey spectra, (b) C 1s, (c) N 1s and (d) Fe 2p.

Both the mass ratio of Fe₃O₄/rGO and the nitrogen-doped carbonization temperature affect the performance of the CO₂RR. As shown in Figure 5, all electrochemical tests were performed in a 0.5 M KHCO₃ solution saturated with CO₂. Three tests were performed at the same time interval at each applied point and then averaged. The prepared catalyst N-Fe₃C/rGO-H produces CO and H₂ as the main products for the reduction of CO₂. The Faraday efficiency at different mass ratios is closely related to the applied potential. Figure 5a depicts the effect of Fe₃O₄/rGO at different mass ratios. It can be observed that the FE_{CO} of N-Fe₃C/rGO-H-100 gradually increases, reaching a maximum value of 40.8% when the potential is from −0.2 to −0.3 V. While at −0.4 to −1.0 V, the FE_{CO} gradually decreases as the potential becomes negative. The CO₂RR and HER are competing reactions; therefore, FE_{H₂} shows the opposite trend. In Figure 5b, FE_{H₂} first decreases sharply to 37.0% at −0.2 to −0.3 V and then progressively increases with increasing potential. The maximum FE potential for the reduction of CO₂ to CO by N-Fe₃C-H was located at −0.5 V, in contrast to the lower catalytic activity and selectivity of rGO for the CO₂RR, indicating that N-Fe₃C/rGO-H can provide the catalytic active site to promote the CO₂RR. Compared to N-Fe₃C/rGO-H (mass ratios of 80 and 120), N-Fe₃C-H and rGO, N-Fe₃C/rGO-H-100 exhibited good activity for the CO₂RR. This is because small loadings do not provide enough catalytic active sites, and too high loadings cause the active sites to accumulate [47].

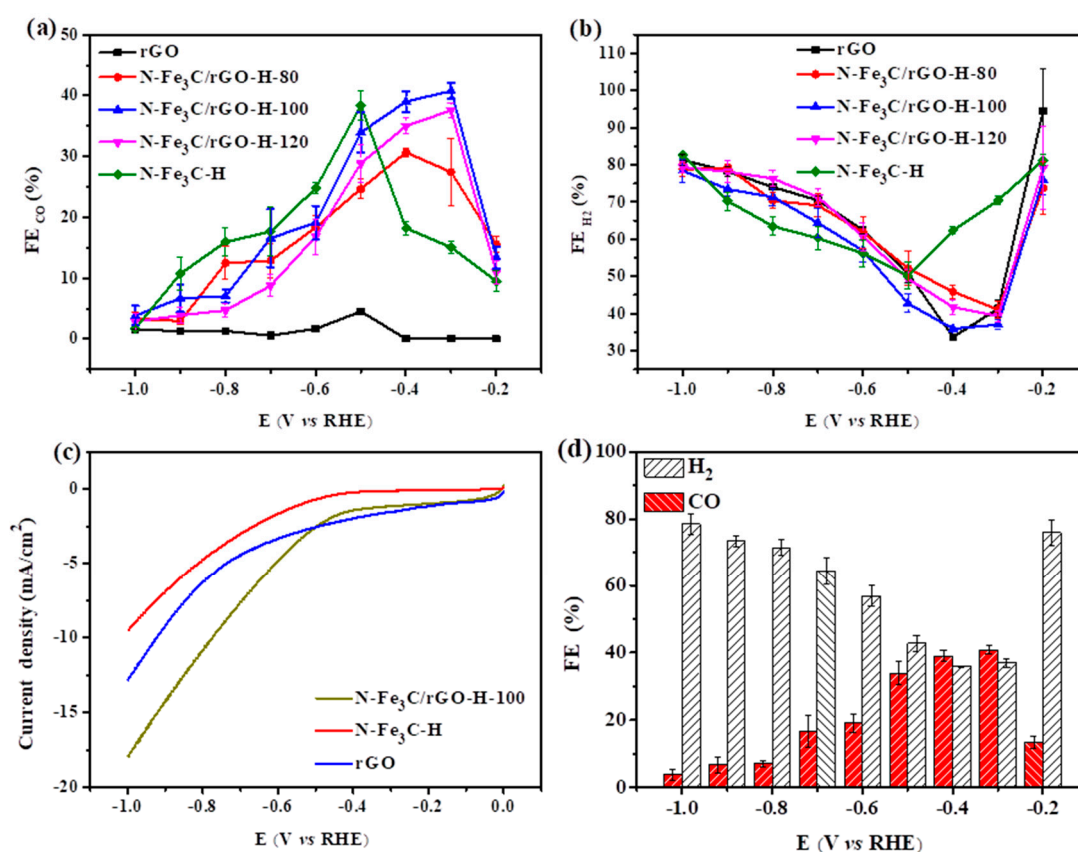


Figure 5. (a,b) Faradaic efficiency of CO and H₂ at different mass ratios; (c) LSV of N-Fe₃C/rGO-H-100, N-Fe₃C-H and rGO; (d) FE of N-Fe₃C/rGO-H-100.

Therefore, N-Fe₃C-H, rGO, and N-Fe₃C/rGO-H-100 were performed by linear scanning voltammetry (LSV) at a sweep rate of 50 mV/s (Figure 5c). N-Fe₃C/rGO-H-100 exhibited positive onset and high current density over the entire potential range tested, indicating its high catalytic activity in the CO₂RR [48,49]; the current density of each catalyst at different potentials was also tested, as shown in Figure S5, and it was found that rGO increased the current density of N-Fe₃C; this also implies that the synergistic results of N-Fe₃C and rGO can improve the catalytic performance. Combined with XPS analysis, it can be speculated that C-N and Fe-N are the catalytic active sites of the CO₂RR. This is because the introduction of N atoms into the carbon substrate provides an optional opportunity to directly tune the electronic structure of the metal centre of the anchored molecular catalyst. The doping of N in the conducting carbon substrate as an axial ligand for the iron centre reduces the electron density of the iron 3D orbitals, thus reducing the Fe-CO π back-donation, facilitating the desorption of CO and improving the electrocatalytic activity and selectivity [50–52]. The bilayer capacitance (Cdl) of the three catalysts was tested using cyclic voltammetry; since the bilayer capacitance is proportional to the electrochemically active specific surface area (ECSA), Cdl can be used to represent the ECSA. The interval without any Faraday potential is selected and tested with different sweeps, as shown in Figure S6. The Cdl values of N-Fe₃C-H, rGO and N-Fe₃C/rGO-H-100 were 5.4, 3.9 and 6.5 mF/cm², respectively. The Cdl of N-Fe₃C/rGO-H-100 was significantly better than that of N-Fe₃C-H and rGO, so its high catalytic activity contributed to having a large ECSA. We investigated the stability of N-Fe₃C/rGO-H-100 for CO₂ reduction at -0.4 V (Figure S7). The FE_{CO} was found to remain at approximately 26% after 12 h, indicating that the catalyst still has high catalytic activity and its morphology remains largely unchanged after a long stability test. As shown in Figure S8, by varying the applied potential (-0.2 to -1.0), the syngas H₂/CO ratio varies from 1 to 20 and was compared with other recently reported

catalysts for syngas preparation (Table S1). It can be clearly shown that the desired syngas ratio can be obtained by adjusting the potential.

We found a suitable $\text{Fe}_3\text{O}_4/\text{rGO}$ mass ratio (100), and, at this mass ratio, the effect of nitrogen doping temperature on the CO_2RR performance was investigated. Figure S9a shows the LSV of $\text{N-Fe}_3\text{C}/\text{rGO-H}$ at different nitrogen doping temperatures. The onset potentials are similar for temperatures of 700 and 800 °C, but the current density of $\text{N-Fe}_3\text{C}/\text{rGO-H-100}$ is slightly higher than that of $\text{N-Fe}_3\text{C}/\text{rGO-H-700}$, as further demonstrated in Figure S9b. To further investigate the effect of temperature on the CO_2RR , electrochemical tests were performed using these three catalysts and compared (Figure S9c,d). The FE_{CO} of $\text{N-Fe}_3\text{C}/\text{rGO-H-100}$ increases and then decreases as the potential becomes negative, reaching a maximum of 40.8% at -0.3 V. Similarly, the corresponding FE_{H_2} decreases to a minimum value of 37.0%. This is because different nitrogen doping temperatures affect the active sites formed between Fe, N and C, and, hence, show variable catalytic properties. The level of nitrogen doping temperature affects the active site of the reaction, and only the right temperature can show the best catalytic performance.

Electrochemical tests reveal that: the assembly of different masses of Fe_3O_4 NPs to rGO for CO_2RR results in a consistent trend of CO generation (FE reaches a maximum at -0.3 V) as shown in Figure S10. The applied potential of the maximum FE corresponding to the reduction of CO_2 to CO by $\text{N-Fe}_3\text{C-H}$ increases (-0.5 V), indicating a lower activity than $\text{N-Fe}_3\text{C}/\text{rGO-H}$. Pure rGO is dominated by the hydrogen evolution reaction.

Based on the above expression, the optimal nitrogen-doped carbonization temperature and mass ratio are 800 °C and 100, with 40.8% and 37.0% FE_{CO} and FE_{H_2} for catalyst $\text{N-Fe}_3\text{C}/\text{rGO-H-100}$ at -0.3 V, respectively (Figure 5d). The reasons for the high performance of $\text{N-Fe}_3\text{C}/\text{rGO-H-100}$ on the CO_2RR are as follows: (1) the high catalytic activity after strong acid etching of part of Fe_3C leaving empty shells on the rGO surface and the interaction between Fe, N and C to regulate the electron and mass transport [26]; (2) the bonding of the metal to the nitrogen site causes an increase in the density of positive charges on the adjacent carbon atoms, which facilitates the doping of the metal Fe-N-C active site [53]; and (3) rGO acts as a catalyst substrate to provide good reaction conditions and improve the conductivity of the reaction.

3. Conclusions

In this study, $\text{N-Fe}_3\text{C}/\text{rGO-H-100}$ was used for the electrocatalytic CO_2 reduction reaction to regulate the syngas ratio. The electrochemical test results showed that the reduction of CO_2 exhibited good activity at lower potentials. At -0.3 V. The Faraday efficiency of CO was 40.8%, and the syngas ratio was adjusted to 1–20 by adjusting the applied potential ($-0.2\sim-1.0$ V); and the total current density reached 29.1 mA/cm^2 at -1.0 V. $\text{N-Fe}_3\text{C}/\text{rGO-H-100}$ has good activity, selectivity and long-term stability at relatively low potentials and can be used as an effective catalyst for the electrocatalytic CO_2 reduction reaction.

Supplementary Materials: The following supporting information can be downloaded at: <https://www.mdpi.com/article/10.3390/nano12152546/s1>, Figure S1. SEM images of (a) $\text{Fe}_3\text{O}_4/\text{rGO-80}$, (b) $\text{Fe}_3\text{O}_4/\text{rGO-100}$, (c) $\text{Fe}_3\text{O}_4/\text{rGO-120}$ and (d) Fe_3O_4 . Figure S2. SEM images of (a) $\text{Fe}_3\text{O}_4/\text{rGO-H-80}$, (b) $\text{Fe}_3\text{O}_4/\text{rGO-H-100}$, (c) $\text{Fe}_3\text{O}_4/\text{rGO-H-120}$ and (d) $\text{Fe}_3\text{O}_4\text{-H}$. Figure S3. XRD patterns of $\text{N-Fe}_3\text{C}/\text{rGO-H}$. Figure S4. Raman spectra of $\text{N-Fe}_3\text{C}/\text{rGO-H-100}$ and rGO. Figure S5. Total current density of $\text{N-Fe}_3\text{C-H}$, rGO and $\text{N-Fe}_3\text{C}/\text{rGO-H-100}$ in CO_2 -saturated 0.5 M KHCO_3 solution. Figure S6. (a–c) Double-layer capacitance of $\text{N-Fe}_3\text{C}/\text{rGO-H-100}$, $\text{N-Fe}_3\text{C-H}$ and rGO; (d) determination of double-layer capacitance over a range of scan rates. Figure S7. (a) Stability of $\text{N-Fe}_3\text{C}/\text{rGO-H-100}$ catalyst at -0.4 V; (b) TEM image after testing stability. Figure S8. $\text{N-Fe}_3\text{C}/\text{rGO-H-100}$ syngas components at different applied potentials. Figure S9. CO_2RR of $\text{N-Fe}_3\text{C}/\text{rGO-H-100}$, $\text{N-Fe}_3\text{C-H}$ and rGO: (a) LSV; (b) total current density; (c,d) Faradaic efficiency of CO and H_2 at different nitrogen doping temperatures (700–900 °C). Figure S10. FECO obtained for $\text{N-Fe}_3\text{C}/\text{rGO-H}$ at -0.3 V. Table S1. The performance comparison of $\text{N-Fe}_3\text{C}/\text{rGO-H-100}$ and other catalysts. References [54–62] are cited in the supplementary materials.

Author Contributions: Formal analysis, T.Y.; investigation, T.Y. and H.H.; writing—original draft preparation, T.Y.; writing—review and editing, Y.C. and J.J.; funding acquisition, M.J.; funding acquisition, Y.C. and J.J. All authors have read and agreed to the published version of the manuscript.

Funding: This research was funded by the Natural Science Foundation of Inner Mongolia of China (2022QN02002), Science and Technology Program of Inner Mongolia Autonomous Region, China (2020PT0003), and the Research Foundation for Advanced Talents of Inner Mongolia Normal University (No. 2018YJRC001 and 2018YJRC012) for funding this study.

Institutional Review Board Statement: Not applicable.

Informed Consent Statement: Not applicable.

Data Availability Statement: Not applicable.

Conflicts of Interest: The authors declare no conflict of interest.

References

1. Xie, H.; Wang, T.; Liang, J.; Li, Q.; Sun, S. Cu-based nanocatalysts for electrochemical reduction of CO₂. *Nano Today* **2018**, *21*, 41–54. [[CrossRef](#)]
2. Kim, S.W.; Park, M.; Kim, H.; Yoon, K.J.; Son, J.W.; Lee, J.H.; Kim, B.K.; Lee, J.H.; Hong, J. In-Situ nano-alloying Pd-Ni for economical control of syngas production from high-temperature thermo-electrochemical reduction of steam/CO₂. *Appl. Catal. B Environ.* **2017**, *200*, 265–273. [[CrossRef](#)]
3. Agarwal, A.S.; Zhai, Y.; Hill, D.; Sridhar, N. The electrochemical reduction of carbon dioxide to formate/formic acid: Engineering and economic feasibility. *ChemSusChem.* **2011**, *4*, 1301–1310. [[CrossRef](#)]
4. Huan, T.N.; Simon, P.; Rousse, G.; Genois, I.; Artero, V.; Fontecave, M. Porous dendritic copper: An electrocatalyst for highly selective CO₂ reduction to formate in water/ionic liquid electrolyte. *Chem. Sci.* **2017**, *8*, 742–747. [[CrossRef](#)] [[PubMed](#)]
5. Zhao, Z.Y.; Chen, Y.L.; Chang, R.D. How to stimulate renewable energy power generation effectively?—China’s incentive approaches and lessons. *Renew. Energy* **2016**, *92*, 147–156. [[CrossRef](#)]
6. Qiao, J.; Liu, Y.; Hong, F.; Zhang, J. A review of catalysts for the electroreduction of carbon dioxide to produce low-carbon fuels. *Chem. Soc. Rev.* **2014**, *43*, 631–675. [[CrossRef](#)]
7. Diercks, C.S.; Liu, Y.; Cordova, K.E.; Yaghi, O.M. The role of reticular chemistry in the design of CO₂ reduction catalysts. *Nat. Mater.* **2018**, *17*, 301–307. [[CrossRef](#)]
8. Chang, B.; Zhang, X.G.; Min, Z.; Lu, W.; Li, Z.; Qiu, J.; Wang, H.; Fan, J.; Wang, J. Efficient electrocatalytic conversion of CO₂ to syngas for the Fischer-Tropsch process using a partially reduced Cu₃P nanowire. *J. Mater. Chem. A* **2021**, *9*, 17876–17884. [[CrossRef](#)]
9. Hernández, S.; Farkhondehfar, M.A.; Sastre, F.; Makkee, M.; Saracco, G.; Russo, N. Syngas production from electrochemical reduction of CO₂: Current status and prospective implementation. *Green Chem.* **2017**, *19*, 2326–2346. [[CrossRef](#)]
10. Lu, S.; Shi, Y.; Meng, N.; Lu, S.; Yu, Y.; Zhang, B. Electrosynthesis of syngas via the Co-reduction of CO₂ and H₂O. *Cell Rep. Phys. Sci.* **2020**, *1*, 100237. [[CrossRef](#)]
11. Wei, B.; Xiong, Y.; Zhang, Z.; Hao, J.; Li, L.; Shi, W. Efficient electrocatalytic reduction of CO₂ to HCOOH by bimetallic In-Cu nanoparticles with controlled growth facet. *Appl. Catal. B Environ.* **2021**, *283*, 119646. [[CrossRef](#)]
12. Hickman, D.A.; Schmidt, L.D. Production of syngas by direct catalytic oxidation of methane. *Science* **1993**, *259*, 343. [[CrossRef](#)] [[PubMed](#)]
13. Nguyen, V.N.; Blum, L. Syngas and synfuels from H₂O and CO₂: Current status. *Chem. Ing. Tech.* **2015**, *87*, 354–375. [[CrossRef](#)]
14. Li, S.; Alfonso, D.; Nagarajan, A.V.; House, S.D.; Yang, J.C.; Kauffman, D.R.; Mpourmpakis, G.; Jin, R. Monopalladium substitution in gold nanoclusters enhances CO₂ electroreduction activity and selectivity. *ACS Catal.* **2020**, *10*, 12011–12016. [[CrossRef](#)]
15. Buckley, A.K.; Cheng, T.; Oh, M.H.; Su, G.M.; Garrison, J.; Utan, S.W.; Zhu, C.; Toste, F.D.; Goddard, W.A.; Toma, F.M. Approaching 100% selectivity at low potential on Ag for electrochemical CO₂ reduction to CO using a surface additive. *ACS Catal.* **2021**, *11*, 9034–9042. [[CrossRef](#)]
16. Jia, L.; Sun, M.; Xu, J.; Zhao, X.; Zhou, R.; Pan, B.; Wang, L.; Han, N.; Huang, B.; Li, Y. Phase-dependent electrocatalytic CO₂ reduction on Pd₃Bi nanocrystals. *Angew. Chem. Int. Ed.* **2021**, *60*, 21741–21745. [[CrossRef](#)]
17. Zhang, T.; Li, X.; Qiu, Y.; Su, P.; Xu, W.; Zhong, H.; Zhang, H. Multilayered Zn nanosheets as an electrocatalyst for efficient electrochemical reduction of CO₂. *J. Catal.* **2018**, *357*, 154–162. [[CrossRef](#)]
18. García, J.; Jiménez, C.; Martínez, F.; Camarillo, R.; Rincón, J. Electrochemical reduction of CO₂ using Pb catalysts synthesized in supercritical medium. *J. Catal.* **2018**, *367*, 72–80. [[CrossRef](#)]
19. Guo, S.; Zhao, S.; Wu, X.; Li, H.; Zhou, Y.; Zhu, C.; Yang, N.; Jiang, X.; Gao, J.; Bai, L.; et al. A Co₃O₄-CDots-C₃N₄ three component electrocatalyst design concept for efficient and tunable CO₂ reduction to syngas. *Nat. Commun.* **2017**, *8*, 1828. [[CrossRef](#)]
20. He, R.; Zhang, A.; Ding, Y.; Kong, T.; Xiao, Q.; Li, H.; Liu, Y.; Zeng, J. Achieving the widest range of syngas proportions at high current density over cadmium sulfoselenide nanorods in CO₂ electroreduction. *Adv. Mater.* **2018**, *30*, 1705872. [[CrossRef](#)]

21. Lv, K.; Teng, C.; Shi, M.; Yuan, Y.; Zhu, Y.; Wang, J.; Kong, Z.; Lu, X.; Zhu, Y. Hydrophobic and electronic properties of the E-MoS₂ nanosheets induced by FAS for the CO₂ electroreduction to syngas with a wide range of CO/H₂ ratios. *Adv. Funct. Mater.* **2018**, *28*, 1802339. [[CrossRef](#)]
22. Zhang, M.; Zhang, Z.; Zhao, Z.; Huang, H.; Anjum, D.H.; Wang, D.; He, J.H.; Huang, K.W. Tunable selectivity for electrochemical CO₂ reduction by bimetallic Cu–Sn catalysts: Elucidating the roles of Cu and Sn. *ACS Catal.* **2021**, *11*, 11103–11108. [[CrossRef](#)]
23. Zou, X.; Ma, C.; Li, A.; Gao, Z.; Shadike, Z.; Jiang, K.; Zhang, J.; Huang, Z.; Zhu, L. Nanoparticle-assisted Ni–Co binary single-atom catalysts supported on carbon nanotubes for efficient electroreduction of CO₂ to syngas with controllable CO/H₂ ratios. *ACS Appl. Energy Mater.* **2021**, *4*, 9572–9581. [[CrossRef](#)]
24. Luna, P.D.; Hahn, C.; Higgins, D.; Jaffer, S.A.; Jaramillo, T.F.; Sargent, E.H. What would it take for renewably powered electrosynthesis to displace petrochemical processes? *Science* **2019**, *364*, 3506. [[CrossRef](#)]
25. Chen, P.; Jiao, Y.; Zhu, Y.H.; Chen, S.M.; Song, L.; Jaroniec, M.; Zheng, Y.; Qiao, S.Z. Syngas production from electrocatalytic CO₂ reduction with high energetic efficiency and current density. *J. Mater. Chem. A* **2019**, *7*, 7675–7682. [[CrossRef](#)]
26. Zhao, J.; Deng, J.; Han, J.; Imhanria, S.; Chen, K.; Wang, W. Effective tunable syngas generation via CO₂ reduction reaction by non-precious Fe–N–C electrocatalyst. *Chem. Eng. J.* **2020**, *389*, 124323. [[CrossRef](#)]
27. Yue, T.; Chang, Y.; Liu, J.; Jia, J.; Jia, M. Fe–Ni nanoparticles on N-doped carbon as catalysts for electrocatalytic reduction of CO₂ to tune CO/H₂ ratio. *ChemElectroChem* **2021**, *8*, 4233–4239. [[CrossRef](#)]
28. Yue, T.; Huang, H.; Chang, Y.; Jia, J.; Jia, M. Controlled assembly of nitrogen-doped iron carbide nanoparticles on reduced graphene oxide for electrochemical reduction of carbon dioxide to syngas. *J. Colloid Interface Sci.* **2021**, *601*, 877–885. [[CrossRef](#)]
29. Wang, C.; Yang, F.; Qiu, T.; Cao, Y.; Zhong, H.; Yu, C.; Li, R.; Mao, L.; Li, Y. Preparation of an efficient Fe/N/C electrocatalyst and its application for oxygen reduction reaction in alkaline media. *J. Electroanal. Chem.* **2018**, *810*, 62–68. [[CrossRef](#)]
30. Yang, X.; Sun, X.; Rauf, M.; Mi, H.; Sun, L.; Deng, L.; Ren, X.; Zhang, P.; Li, Y. N-Doped porous tremella-like Fe₃C/C electrocatalysts derived from metal-organic frameworks for oxygen reduction reaction. *Dalton Trans.* **2020**, *49*, 797–807. [[CrossRef](#)]
31. Prslja, P.; López, N. Stability and Redispersion of Ni nanoparticles supported on N-doped carbons for the CO₂ electrochemical reduction. *ACS Catal.* **2020**, *11*, 88–94. [[CrossRef](#)]
32. Shinagawa, T.; Larrazábal, G.O.; Martín, A.J.; Krumeich, F.; Pérez-Ramírez, J. Sulfur-modified copper catalysts for the electrochemical reduction of carbon dioxide to formate. *ACS Catal.* **2018**, *8*, 837–844. [[CrossRef](#)]
33. Zhang, J.; Guo, Y.; Shang, B.; Fan, T.; Lian, X.; Huang, P.; Dong, Y.; Chen, Z.; Yi, X. Unveiling the synergistic effect between graphitic carbon nitride and Cu₂O toward CO₂ electroreduction to C₂H₄. *ChemSusChem* **2021**, *14*, 929–937. [[CrossRef](#)]
34. Park, J.; An, K.; Wang, Y.H.; Park, J.G.; Noh, H.J.; Kim, J.Y.; Park, J.H.; Hwang, N.M.; Hyeon, T. Ultra-large-scale syntheses of monodisperse nanocrystals. *Nat. Mater.* **2004**, *3*, 891–895. [[CrossRef](#)] [[PubMed](#)]
35. Wang, D.W.; Chen, Z.G.; Lu, G.Q.; Cheng, H.M. Synthesis and electrochemical property of boron-doped mesoporous carbon in supercapacitor. *Chem. Mater.* **2008**, *20*, 7195–7200. [[CrossRef](#)]
36. Choi, C.H.; Park, S.H.; Woo, S.I. N-doped carbon prepared by pyrolysis of dicyandiamide with various MeCl₂·xH₂O (Me=Co, Fe, and Ni) composites: Effect of type and amount of metal seed on oxygen reduction reactions. *Appl. Catal. B Environ.* **2012**, *120*, 123–131. [[CrossRef](#)]
37. Wang, Z.; Ang, J.; Liu, J.; Ma, X.Y.D.; Kong, J.; Zhang, Y.; Yan, T.; Lu, X. FeNi alloys encapsulated in N-doped CNTs-tangled porous carbon fibers as highly efficient and durable bifunctional oxygen electrocatalyst for rechargeable zinc-air battery. *Appl. Catal. B Environ.* **2020**, *263*, 118344. [[CrossRef](#)]
38. Silva, W.O.; Silva, G.C.; Webster, R.F.; Benedetti, T.M.; Tilley, R.D.; Ticianelli, E.A. Electrochemical reduction of CO₂ on nitrogen-doped carbon catalysts with and without Iron. *ChemElectroChem* **2019**, *6*, 4626–4636. [[CrossRef](#)]
39. Ju, W.; Bagger, A.; Hao, G.P.; Varela, A.S.; Sinev, I.; Bon, V.; Cuenya, B.R.; Kaskel, S.; Rossmeisl, J.; Strasser, P. Understanding activity and selectivity of metal-nitrogen-doped carbon catalysts for electrochemical reduction of CO₂. *Nat. Commun.* **2017**, *8*, 944. [[CrossRef](#)]
40. Matanovic, I.; Artyushkova, K.; Atanassov, P. Understanding PGM-free catalysts by linking density functional theory calculations and structural analysis: Perspectives and challenges. *Curr. Opin. Electrochem.* **2018**, *9*, 137–144. [[CrossRef](#)]
41. Zhao, X.; Pachfule, P.; Li, S.; Langenhahn, T.; Ye, M.; Tian, G.; Schmidt, J.; Thomas, A. Silica-templated covalent organic framework-derived Fe–N-doped mesoporous carbon as oxygen reduction electrocatalyst. *Chem. Mater.* **2019**, *31*, 3274–3280. [[CrossRef](#)]
42. Ahn, S.H.; Yu, X.; Manthiram, A. “Wiring” Fe–N_x-embedded porous carbon framework onto 1D nanotubes for efficient oxygen reduction reaction in alkaline and acidic media. *Adv. Mater.* **2017**, *29*, 1606534. [[CrossRef](#)] [[PubMed](#)]
43. Liu, J.; Liu, Y.; Li, P.; Wang, L.; Zhang, H.; Liu, H.; Liu, J.; Wang, Y.; Tian, W.; Wang, X.; et al. Fe–N-doped porous carbon from petroleum asphalt for highly efficient oxygen reduction reaction. *Carbon*. **2018**, *126*, 1–8. [[CrossRef](#)]
44. Jiang, W.J.; Gu, L.; Li, L.; Zhang, Y.; Zhang, X.; Zhang, L.J.; Wang, J.Q.; Hu, J.S.; Wei, Z.; Wan, L.J. Understanding the high activity of Fe–N–C electrocatalysts in oxygen reduction: Fe/Fe₃C nanoparticles boost the activity of Fe–N_x. *J. Am. Chem. Soc.* **2016**, *138*, 3570–3578. [[CrossRef](#)]
45. Wei, J.; Liang, Y.; Hu, Y.; Kong, B.; Simon, G.P.; Zhang, J.; Jiang, S.P.; Wang, H. A versatile iron-tannin-framework ink coating strategy to fabricate biomass-derived iron carbide/Fe–N-carbon catalysts for efficient oxygen reduction. *Angew. Chem. Int. Ed.* **2016**, *55*, 1355–1359. [[CrossRef](#)] [[PubMed](#)]

46. Xiao, M.; Zhu, J.; Feng, L.; Liu, C.; Xing, W. Meso/macroporous nitrogen-doped carbon architectures with iron carbide encapsulated in graphitic layers as an efficient and robust catalyst for the oxygen reduction reaction in both acidic and alkaline solutions. *Adv. Mater.* **2015**, *27*, 2521–2527. [[CrossRef](#)]
47. Kolobova, E.; Pakrieva, E.; Pascual, L.; Corberán, V.C.; Bogdanchikova, N.; Farias, M.; Pstryakov, A. Selective oxidation of n-octanol on unmodified and La-modified nanogold catalysts: Effect of metal content. *Catal. Today* **2019**, *333*, 127–132. [[CrossRef](#)]
48. Fan, L.; Xia, Z.; Xu, M.; Lu, Y.; Li, Z. 1D SnO₂ with wire-in-tube architectures for highly selective electrochemical reduction of CO₂ to C1 products. *Adv. Funct. Mater.* **2018**, *28*, 1706289. [[CrossRef](#)]
49. Lu, Y.; Han, B.; Tian, C.; Wu, J.; Geng, D.; Wang, D. Efficient electrocatalytic reduction of CO₂ to CO on an electrodeposited Zn porous network. *Electrochem. Commun.* **2018**, *97*, 87–90. [[CrossRef](#)]
50. Zhang, H.; Li, J.; Xi, S.; Du, Y.; Hai, X.; Wang, J.; Xu, H.; Wu, G.; Zhang, J.; Lu, J.; et al. A graphene-supported single-atom FeN₅ catalytic site for efficient electrochemical CO₂ reduction. *Angew. Chem. Int. Ed.* **2019**, *58*, 14871–14876. [[CrossRef](#)]
51. Yang, X.; Cheng, J.; Xuan, X.; Liu, N.; Liu, J. Boosting defective carbon by anchoring well-defined atomically dispersed Ni-N₄ sites for electrocatalytic CO₂ reduction. *ACS Sustain. Chem. Eng.* **2020**, *8*, 10536–10543. [[CrossRef](#)]
52. Gong, S.; Wang, W.; Xiao, X.; Liu, J.; Wu, C.; Lv, X. Elucidating influence of the existence formation of anchored cobalt phthalocyanine on electrocatalytic CO₂-to-CO conversion. *Nano Energy.* **2021**, *84*, 105904. [[CrossRef](#)]
53. Kim, M.; Yoo, J.M.; Ahn, C.Y.; Jang, J.H.; Son, Y.J.; Shin, H.; Kang, J.; Kang, Y.S.; Yoo, S.J.; Lee, K.S.; et al. Rational generation of Fe-N_x active sites in Fe-N-C electrocatalysts facilitated by Fe-N coordinated precursors for the oxygen reduction reaction. *ChemCatChem.* **2019**, *11*, 5982–5988. [[CrossRef](#)]
54. Chen, K.; Deng, J.; Zhao, J.; Liu, X.; Imhanria, S.; Wang, W. Electrocatalytic production of tunable syngas from CO₂ via a metal-free porous nitrogen-doped carbon. *Ind. Eng. Chem.* **2021**, *60*, 7739–7745. [[CrossRef](#)]
55. Cho, M.; Seo, J.W.; Song, J.T.; Lee, J.Y.; Oh, J. Silver nanowire/carbon sheet composites for electrochemical syngas generation with tunable H₂/CO ratios. *ACS Omega* **2017**, *2*, 3441–3446. [[CrossRef](#)]
56. Daiyan, R.; Chen, R.; Kumar, P.; Bedford, N.M.; Qu, J.; Cairney, J.M.; Lu, X.; Amal, R. Tunable syngas production through CO₂ electroreduction on cobalt-carbon composite electrocatalyst. *ACS Appl. Mater. Interfaces* **2020**, *12*, 9307–9315. [[CrossRef](#)]
57. Kumar, B.; Brian, J.P.; Atla, V.; Kumari, S.; Bertram, K.A.; White, R.T.; Spurgeon, J.M. Controlling the product syngas H₂:CO ratio through pulsed-bias electrochemical reduction of CO₂ on copper. *ACS Catal.* **2016**, *6*, 4739–4745. [[CrossRef](#)]
58. Leverett, J.; Daiyan, R.; Gong, L.; Iputera, K.; Tong, Z.; Qu, J.; Ma, Z.; Zhang, Q.; Cheong, S.; Cairney, J.; et al. Designing undercoordinated Ni-N_x and Fe-N_x on holey graphene for electrochemical CO₂ conversion to syngas. *ACS Nano.* **2021**, *15*, 12006–12018. [[CrossRef](#)]
59. Xie, H.; Chen, S.; Ma, F.; Liang, J.; Miao, Z.; Wang, T.; Wang, H.L.; Huang, Y.; Li, Q. Boosting tunable syngas formation via electrochemical CO₂ reduction on Cu/In₂O₃ core/shell nanoparticles. *ACS Appl. Mater. Interfaces* **2018**, *10*, 36996–37004. [[CrossRef](#)]
60. Zhao, Y.; Miao, Z.; Wang, F.; Liang, M.; Liu, Y.; Wu, M.; Diao, L.; Mu, J.; Cheng, Y.; Zhou, J. N-doped carbon-encapsulated nickel on reduced graphene oxide materials for efficient CO₂ electroreduction to syngas with potential-independent H₂/CO ratios. *J. Environ. Chem. Eng.* **2021**, *9*, 106705. [[CrossRef](#)]
61. Wang, M.; Torbensen, K.; Salvatore, D.; Ren, S.; Joulie, D.; Dumoulin, F.; Mendoza, D.; Lassalle-Kaiser, B.; Isci, U.; Berlinguette, C.P.; et al. CO₂ electrochemical catalytic reduction with a highly active cobalt phthalocyanine. *Nat. Commun.* **2019**, *10*, 3602. [[CrossRef](#)] [[PubMed](#)]
62. Malik, K.; Rajbongshi, B.M.; Verma, A. Syngas production from electrochemical reduction of CO₂ at high current density using oxide derived Zn/Cu nanocomposite. *J. CO₂ Util.* **2019**, *33*, 311–319. [[CrossRef](#)]